ACS OMEGA

Open Access

http://pubs.acs.org/journal/acsodf

Article

Preparation of Novel C/N-Doped $LaFeO_3$ Type Perovskite for Efficient Photocatalytic Degradation of Sodium Humate

Pengcheng Hao, Yanli Suo, Rui Shi, Juan Zhang, Bo Li, Zhen Yan, Jing Wang, Bo Liu, Zhongzhi Wang,* and Xin Qiao*

Cite This: *ACS Omega* 2023, 8, 41744−41754

Read Online

ACCESS | Metrics & More | Article Recommendations | Supporting Information

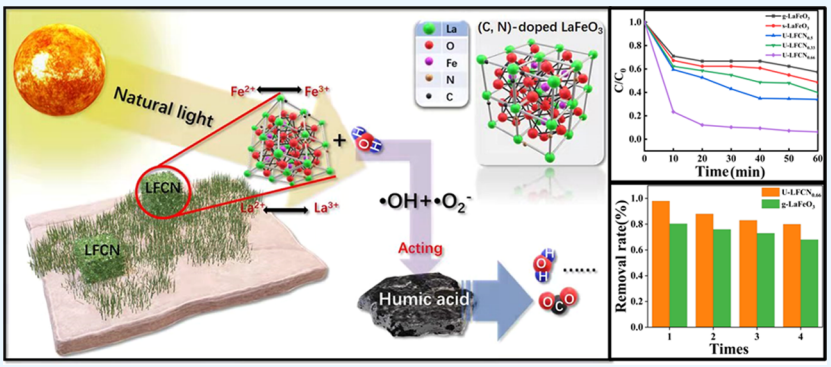

ABSTRACT: $LaFeO_3$ chalcocite precursor was prepared by solid-phase milling method, and $LaFeO_3$-type chalcocite composite catalyst, referred to as LFCN catalyst, was synthesized by in situ doping of carbon and nitrogen (urea, melamine, dicyandiamide, and carbon powder), The catalytic performance of the catalysts was investigated by the different mass ratios of $LaFeO_3$ chalcocite precursor and carbon and nitrogen (1:1, 1:2, and 2:1) and the degradation mechanism. Various characterization analyses, such as X-ray diffraction (XRD), scanning electron microscopy (SEM), transmission electron microscopy (TEM), and Brunauer−Emmett−Teller (BET), showed that the doped composite LFCN catalysts exhibited a hemispherical network structure with a larger specific surface area than that of the pure phase $LaFeO_3$ material. In addition, the $LaFeO_3$ material adjusted the electronic structure of the original $LaFeO_3$ chalcogenide material to a certain extent after in situ doping with organic C and N elements, which enhanced its lattice oxygen oxidation ability. In the study of the catalytic degradation of sodium humate solution under natural light conditions, the catalytic performance was significantly improved compared to that of the pure phase $LaFeO_3$, and 10 mg of the catalyst degraded 30 mg/L of sodium humate solution in 50 min, with a degradation rate increasing from 40 to 98%. The degradation rate increased from 40 to 98% after 4 applications, indicating that the LFCN catalyst has good stability and significant catalytic degradation performance.

1. INTRODUCTION

Humic acids, a major component of natural organic carbon resources, are formed naturally through microbial biodegradation of plant and animal residues and are commonly found in media in which organic matter decomposes, such as water,[1,2] soil,[3] sediments, and organic wastes.[4,5] In fact, it has also been recognized that the presence of humic acids in untreated water inhibits the oxidative degradation of other target contaminants through competitive reactions and produces toxic disinfection byproducts during conventional chlorination disinfection.[6] Consequently, the need to eliminate the water pollutant nature of humic acid in view of its high distribution in aqueous environments has attracted much attention.[7] To date, the main methods used for the removal of humic acids from water bodies include adsorption such as activated carbon type adsorption, advanced oxidation, and photocatalytic degradation.[8−10] Among them, new catalytic materials for oxidative degradation of humic acid and other oxidative degradation that are easy to prepare, structurally stable, with strong catalytic properties and easy to regenerate are a challenging task.[11]

In recent years, chalcogenide (ABO_3)-type materials have attracted a lot of scientific and applied attention in the field of photocatalysis due to their properties such as low price, adaptability, and thermal stability.[12] For example, $LaFeO_3$ has excellent catalytic activity in the photocatalytic degradation of organic matter due to its wide band gap, high chemical

Received: August 19, 2023
Revised: October 5, 2023
Accepted: October 6, 2023
Published: October 26, 2023

stability, nontoxicity, nonharmfulness, and excellent visible light response.[1,13] Among them, hybridized $LaFeO_3$-like materials such as TiO_2-coupled N-doped porous perovskite $LaFeO_3$ have excellent visible photocatalytic activity, whereas Co-doped $LaFeO_3$ is an excellent advanced oxidation (AOPs) catalyst for the efficient oxidative degradation of organic matter by activated monopersulfate.[14,15] The construction of heterojunction classes such as $NiS/LaFeO_3$[16] and $LaFeO_3@TiO_2$[17] has been recently reported to be efficient $LaFeO_3$-based catalysts for photocatalytic degradation of dyestuffs.[18] These studies show great potential for the photocatalytic activity of doped modified $LaFeO_3$. However, the above modified materials have the following drawbacks: they are all metal-containing raw materials, which are difficult to be popularized due to the limitation of the types, and the cost of raw materials;[19,20] as well as the preparation of $LaFeO_3$ nanoparticles requires high temperatures (700−1000 °C high-temperature calcination). In addition, the codoping of nonmetallic elements in semiconductor photocatalysts has become a new direction, and due to the synergistic effect between the two dopants, the codoped catalysts have a stronger visible light absorption capacity than those doped with a single element, which can effectively improve the photocatalytic performance.[21] Therefore, the development of $LaFeO_3$ chalcogenide hybridized materials with nonmetallic elements such as C and N elements is an important strategy to solve the above problems.[21−2223] In particular, the preparation of novel nonmetal-doped $LaFeO_3$ chalcogenide nanoparticles to trap humic acid-based pollutants in water is more challenging.[24]

Here, we report on the preparation of $LaFeO_3$ chalcocite (LFCN) with urea, melamine, and dicyandiamide as C and N source references using a combination of solid-phase milling in situ doping and low-temperature roasting methods and investigate its behavior, such as the degradation of humic acid in artificially configured aqueous humic acid solutions. The effects of C/N doping on the structure and catalytic performance of LFCN catalysts were also investigated. The structure, morphology, and optical properties of the samples were also analyzed by X-ray diffraction (XRD), scanning electron microscopy (SEM), transmission electron microscopy (TEM), and electrochemical tests. Finally, the possible degradation mechanisms were speculated and analyzed by free radical trapping experiments and EPR tests. The synthetic routes and results of the materials reported in this work will provide new ideas for the application of chalcogenide materials in the field of catalytic degradation of organic pollutants in water.

2. CATALYST PREPARATION

2.1. Preparation of $LaFeO_3$ Precursors. The traditional preparation method was used.[25] $La(NO_3)_3{\cdot}6H_2O$ (0.433 g, 1.0 mmol), $Fe(NO_3)_3{\cdot}9H_2O$ (0.404 g, 1.0 mmol), and citric acid (0.420 g, 2.0 mmol) according to the mass ratio of 1:1:2 were placed in a 100 mL beaker, and 30 mL of deionized water was added to fully dissolve the solution by stirring for 4 h and then dried at 80 °C until the solution dried to a reddish brown gel. In the solid-phase milling method, without adding deionized water, the raw materials (as above for ingredients) were added to the mortar one by one and milled for 30 min until the samples were in the form of reddish brown gel and dried at 120 °C in an oven to obtain the $LaFeO_3$ chalcogenide precursor.

2.2. Preparation of $LaFeO_3$. The prepared $LaFeO_3$ calcium titanium ore precursor was ground into powder form uniformly and placed in a ceramic crucible, which was placed in a muffle furnace for calcination. The initial temperature was set to 25 °C; with a heating rate of 3 °C/min, the temperature was raised to 170 °C and held for 2 h for the water to evaporate to dryness. Then, the temperature was further increased to 500, held for 4 h to ensure that the reaction was sufficient, and ultimately increased to 700 °C to bake the mixture for 6 h, which was then cooled to room temperature. The products were taken out one by one, ground to powder form, and collected to obtain the $LaFeO_3$ calcium titanium ore.

2.3. Preparation of C/N-Doped $LaFeO_3$ Chalcogenide Composites. The composite catalysts were synthesized by the solid-phase milling modified sol−gel method and calcination method (Scheme 1). $LaFeO_3$ precursor (1 g) and CH_2N_2O (2 g) were added to the mortar and milled uniformly and then calcined at high temperature in a muffle furnace (heating procedure: 170 °C for 2 h, then 500 °C for 4 h, then 700 °C for 6 h at a temperature rate of 3 °C/min); the composite catalyst with optimum catalytic performance was collected after cooling and recorded as U-LFCN0.66 (Prefix letters such as U is the first letter of the English capitalization of urea, subscripts such as 0.66 is based on the C/N source in the total proportion of raw materials, and the full text of the preparation of the sample subscripts are based on this basis for labeling.).

Scheme 1. Schematic Diagram of Sample Synthesis Process

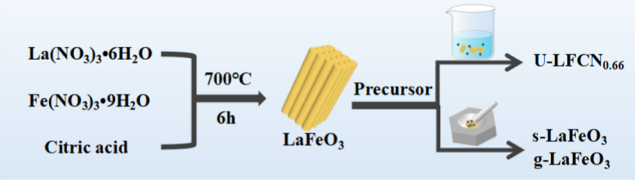

The catalysts with different doping amounts were prepared by varying the amount of CH_2N_2O added (m precursor/m organics = 1:1, 2:1) and were denoted as U-LFCN0.5 and U-LFCN0.33. The composites were obtained by using melamine, dicyandiamide, and graphite instead of urea with the doping amount of m precursor/m organics = 1:2 and were denoted as M-LFCN0.66, D-LFCN0.66, and G-LFCN0.66, respectively. Pure phase $LaFeO_3$ chalcogenides were prepared by the sol−gel method and the solid-phase milling method and were denoted as g-$LaFeO_3$ and s-$LaFeO_3$, respectively.

3. RESULTS AND DISCUSSION

3.1. Chemical Structure of Catalysts. XRD characterization analyses (Figure 1) were carried out on different LFCN catalysts separately, with the aim of investigating whether their structures were changed or not. Figure 1a shows the full XRD spectra of LFCN with different doping amounts from which it can be found that both the solid-phase milling and the sol−gel method can finally obtain the corresponding ABO_3-type chalcogenide structure. Compared to the sol−gel method, the diffraction peaks of chalcocite (U-$LaFeO_3$) prepared by solid-phase milling are stronger in intensity, which may be related to the synthesis method in which the metal salts are squeezed by the mechanical force of milling during solid-phase synthesis, resulting in a higher degree of crystallinity after sintering.[26] Meanwhile, it can be learned from the full spectrum that after doping with organic elements, the

https://doi.org/10.1021/acsomega.3c06161
ACS Omega 2023, 8, 41744−41754

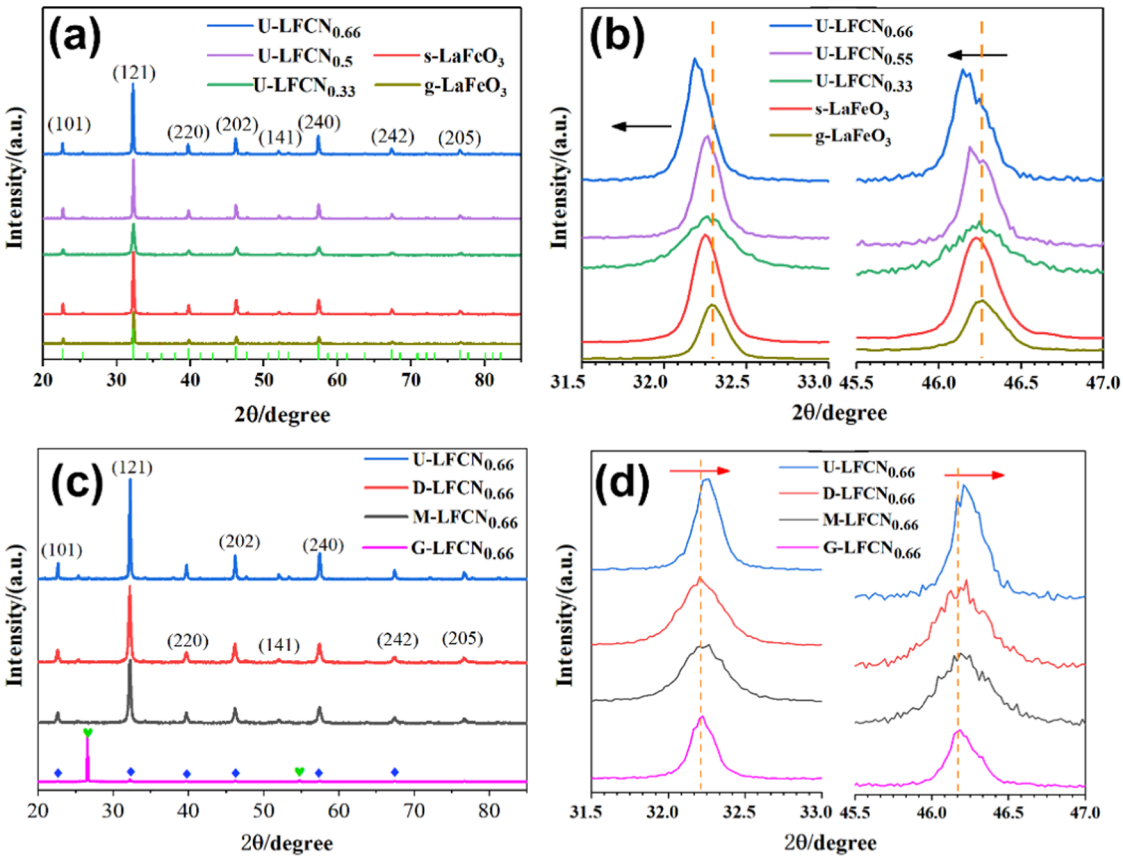

Figure 1. XRD spectra of different catalysts: (a, c) full spectrum; (b, d) partial magnification.

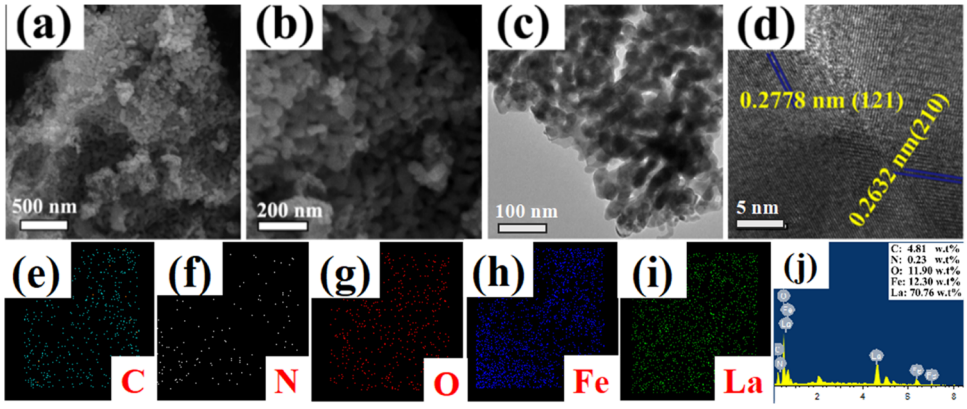

Figure 2. (a, b) SEM images of U-LFCN0.66. (c, d) TEM images of U-LFCN0.66. (e–j) EDX elemental surface scan energy spectra of U-LFCN0.66.

composites still maintain the characteristic ABO_3-type structure of chalcogenide. However, from Figure 1b, it can be found that the peak and positions of the composites at the (121) and (202) crystal planes were shifted after organic doping, which may be related to the change in the dopant size.[27,28] Moreover, the higher the amount of N doping, the more obvious the shift is, which may be due to the distortion of the crystal planes caused by N doping. This shift in the peak position may lead to a certain degree of lattice defects, which in turn expose more active interfaces at the oxygen vacancy sites in the chalcogenides,[27,28] which is intrinsically conducive to the enhancement of the catalyst activity, which is consistent with the difference in catalytic activity of the catalysts in the catalytic activity test,[29−3031] i.e., the higher the amount of N doping the more pronounced rightward shift of the peak positions of the major crystal planes is positively correlated with their catalytic degradation effects.[32] This is a very interesting phenomenon, the different preparation methods and organic elements doping amount, although did not directly change the intrinsic structure of the chalcogenide materials but can be adjusted to some extent the crystalline state of the composites and photoelectronic effect.

Figure 1c shows the XRD patterns of LFCN composites prepared by doping with different organics. It can be seen that the different carbon and nitrogen sources also do not affect the ABO_3-type structure, and the characteristic peaks of the distinct chalcogenide structure appear in all composites, including graphite-doped materials. The composites prepared

https://doi.org/10.1021/acsomega.3c06161
ACS Omega 2023, 8, 41744−41754

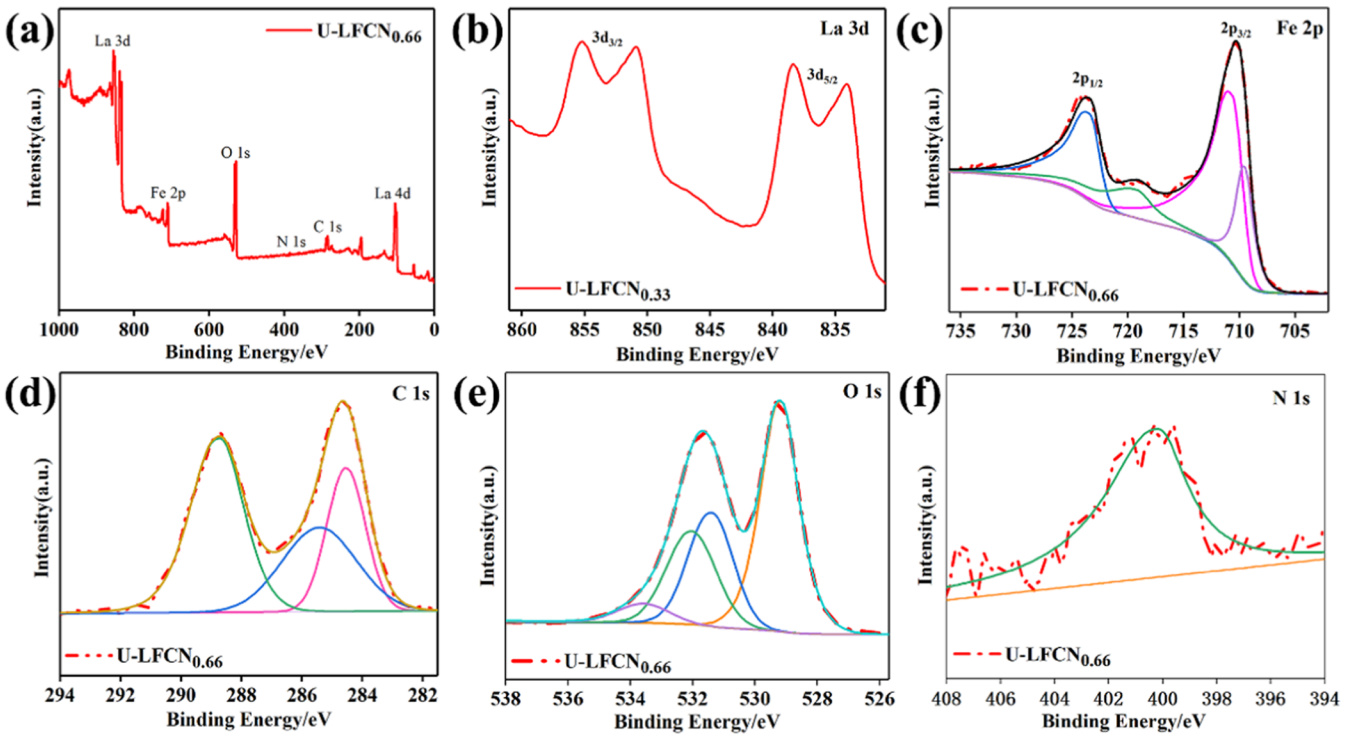

Figure 3. XPS spectra of U-LFCN0.66: (a) full spectrum; (b) La 3d; (c) Fe 2p; (d) C 1s; (e) O 1s; and (f) N 1s.

with graphite doping showed a particularly strong diffraction peak at 26.5°, which was attributed to the (002) crystallographic peak.[21] The reason for this peak may be that the main substance in graphite is elemental C. The pure phase of elemental C is not oxidized to CO_2 during sintering but still retains a large amount of elemental C, which reforms at high temperatures and thus exhibits a sharp peak. From Figure 1d, which is a partial enlargement of the composites doped with different organics, it can be seen that the materials of graphite, melamine, and dicyandiamide are shifted in the (121) and (202) crystal planes, indicating that the electronic structure of LFCN materials can be adjusted by the different organic C and N elements and the doping of different organics, this affects the catalytic activity of the catalyst.

3.2. Morphological Characterization of Catalysts. Usually, the catalytic activity of a catalyst is directly related to its morphology since all oxidation−reduction reactions take place at the catalyst interface. For this reason, the material with the best catalytic performance, U-LFCN0.66, was characterized using SEM, TEM, and EDX elemental surface scanning energy spectroscopy. As can be seen from Figure 2a,b, the U-LFCN0.66 catalyst has a nanoparticle structure consisting of many regular cylindrical nanorods of about 200 nm that are stacked and aggregated. The surface shows many irregular stacked pores, which are relatively stable because they are fused and connected by some neighboring nanoparticles during the sintering preparation. Figure 2c,d shows high-resolution transmission electron micrographs of the U-LFCN0.66 catalyst. The short rodlike structure of the U-LFCN0.66 catalyst can be seen. The U-LFCN0.66 catalyst can be seen to have obvious lattice stripes in the high-resolution transmission, and the lattice spacings of 0.2612 and 0.2774 nm correspond to the (210) and (121) crystal planes of the $LaFeO_3$ material,[18] respectively. This also once again confirms that the U-LFCN0.66 catalyst maintains the characteristic structure of the ABO_3-type chalcogenide materials. In addition, Figure 2e−j shows the surface scanning EDX elemental spectra of the U-LFCN0.66 material, which shows that the La, Fe, O, C, and N elements are uniformly dispersed in the material; especially, the C and N elements do not appear to be localized aggregation phenomena. This indicates that unlike the traditional composite heterojunction materials, the small amount of O, C, and N elements in the organic carbon- and nitrogen-doped LFCN catalysts prepared by the in situ one-pot method plays a role in regulating the microenvironment of the electronic structure of the material. U-LFCN0.66 still has the characteristic structure of 1:1:3 ABO_3-type chalcogenides (Figure 2j).

3.3. XPS Testing of Catalysts. X-ray photoelectron spectroscopy (XPS) analysis of the U-LFCN0.66 catalyst was performed to determine the elemental composition and chemical oxidation state of the sample surface. Complete and detailed spectra of La 3d, Fe 2p, O 1s, C 1s, and N 1s were obtained. From Figure 3b, it can be seen that the main peaks at 833.6 and 850.6 eV can be attributed to La $3d_{5/2}$ and La $3d_{3/2}$ of the trivalent state of the La ions, whereas the satellite peaks at 837.8 and 854.7 eV can be attributed to charge transfer from the ligand O 2p energy level to the La 4f energy level. The two major peaks at 724.2 and 710.3 eV with vibrational satellites at 718.6 eV found in the XPS spectra of Fe 2p in Figure 3c can be assigned to Fe $2p_{1/2}$ and Fe $2p_{3/2}$,[33−35] indicating that both Fe and lanthanide ions are present in the chemical valence state +3. In addition to the different La, Fe, and O spectral lines, Figure 3d shows the C 1s signal, and the XPS spectrum can be divided into three sets of peaks, with the peaks located at 284.8 and 286 eV corresponding to the C−C bond and the oxygen-bound material produced from indeterminate carbon. The third peak located at 288.7 eV can be attributed to lanthanum carbonate produced by the reaction of CO_2 (formed by the combustion process) with the lanthanum oxide surface during

https://doi.org/10.1021/acsomega.3c06161
ACS Omega 2023, 8, 41744−41754

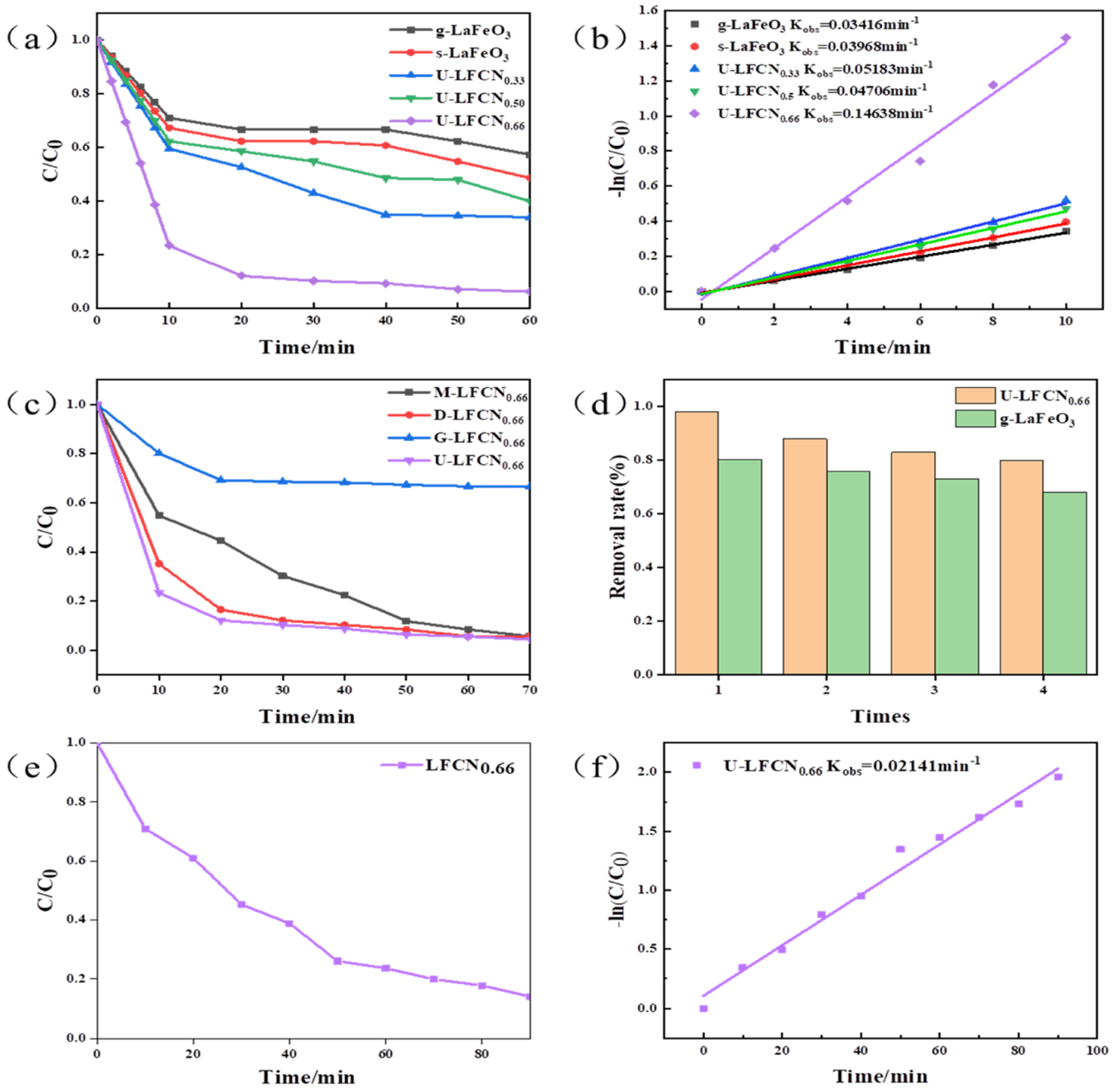

Figure 4. (a) Degradation rate of sodium humate by different catalysts. (b) Sequential kinetic response of sodium humate removal by different catalysts. (c) Degradation rate of sodium humate by different C/N source catalysts. (d) Degradation rate of repeated experiments. (e) Amplified degradation rate of sodium humate by the U-LFCN0.66 catalyst. (f) Sequential kinetic response of sodium humate by the U-LFCN0.66 catalyst.

the formation of $LaFeO_3$.[36] Figure 3e shows the O 1s signals for oxygen molecules with binding energies of about 529.9 eV lattice oxygen, 531.1 eV oxygen vacancies, and 532.0 eV surface adsorbed oxygen molecules, which correspond to the main signals for the contributions from La−O and Fe−O lattice bonds, some surface hydroxyl groups, and chemisorbed water. Consistent with the expected composition among La, Fe, and O, the atomic ratio was found to be about 1:1:3 by comparing the relative signal intensities in different XPS spectra. Figure 3f shows the N 1s signals with a binding energy of about 400.18 eV, which corresponds to the main signals of the C−NH_2 lattice bonds.[24]

3.4. Degradation Performance Testing of Catalysts.

Humic acid, which has large-sized molecules and is difficult to degrade, was selected as a typical organic pollutant to investigate the catalytic activity of the U-LFCN0.66 catalyst in aqueous solution. It is very interesting to note that unlike other carbon-based catalysts or inorganic oxide materials, the U-LFCN0.66 catalyst does not require the promotion of an external light source during the degradation of sodium humate. Under natural light conditions, it still had strong catalytic activity. This indicates that the U-LFCN0.66 catalyst itself has strong oxidizing properties. The results are shown in Figure 4a. It can be found that the catalytic performance of the materials prepared by either the solid-phase method or the sol−gel

https://doi.org/10.1021/acsomega.3c06161
ACS Omega 2023, 8, 41744−41754

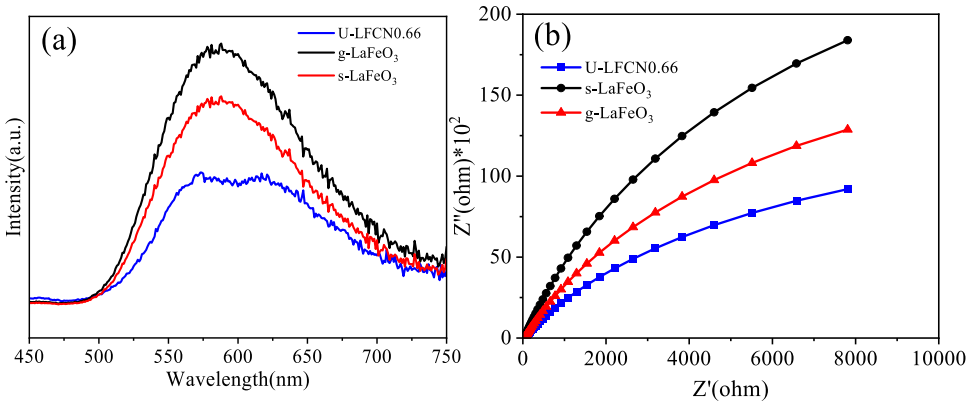

Figure 5. (a) Photoluminescence (PL) and (b) EIS mapping of different catalysts.

method is unsatisfactory (g-$LaFeO_3$: 40%, s-$LaFeO_3$: 34%), which suggests that although the $LaFeO_3$ material has a certain oxidizing ability of its own,[37] and this is not enough to induce the sodium humate solution to complete the oxidative degradation. The catalytic effects of the composites obtained by doping with organic matter were all stronger than those of the undoped materials. When the amount of organic matter doping is gradually increased, the catalytic activity of the catalyst material is more obvious, and finally, the catalyst material of U-LFCN0.66 has the best reaction performance, and the degradation rate of sodium humate reaches 98%, which is 2.88 times higher than that of the pure phase chalcocite material. As shown in Figure 4b, the analysis of the first 10 min kinetic experiments showed that the reaction rate constant (k) of U-LFCN0.66 was calculated to be 0.14638 min^{-1}, which is about 4 times higher than that of g-$LaFeO_3$. Meanwhile, the effects of different doping sources on the catalytic performance of LFCN catalysts were explored, and the results are shown in Figure 4c. The catalytic activity of g-LFCN0.66 obtained from composites using graphite as the doping element showed little performance enhancement compared to the undoped pure phase material, which proved that the C element alone is not the main influencing factor. The catalytic performance of the material was significantly improved when doped with dicyandiamide and melamine (60 min, 89%). It can be hypothesized that the introduction of the N element is the key to enhancing the oxidative degradation ability of the materials. However, after comparing different nitrogen source doping, it was found that the catalytic performance of the composites obtained from urea as dopant was still the best, which may be related to the structure of urea and its small amount of oxygen, although the material preparation process was sintered in a muffle furnace and completely exposed to the air atmosphere, but the oxygen element in the sintering process could not completely replace the oxygen in the structure of the material itself.[38] In conclusion, the doping of organic carbon and nitrogen elements effectively improved the catalytic performance of $LaFeO_3$ materials.

The results of the reusability of the U-LFCN0.66 composite catalyst and the scaled-up reaction are shown in Figure 4d,e. The reusability of the catalyst largely determines the value of the catalyst.[39] From Figure 4d, it can be seen that the degradation rate of the U-LFCN0.66 catalyst on sodium humate solution can still reach more than 80% after 4 times of reuse. After the reaction was scaled up by a factor of 12.5, the catalytic performance of the U-LFCN0.66 material could still reach more than 95% (Figure 4e). In addition, kinetic experimental analysis of the entire degradation process showed that the calculated amplification reaction rate constant (k) for U-LFCN0.66 was 0.02141 min^{-1}, which is more in line with the first-order kinetics compared to those of the small-dose experiments. The U-LFCN0.66 material showed promising catalytic activity and stability in replicated experiments and scaled-up production, which opens up the possibility of its application in practical production.

3.5. Electrochemical Performance Testing of Catalysts. Fluorescence emission spectroscopy (PL) is an important characterization tool used to elucidate the efficiency of photoexcited electron capture, migration, transfer, and separation in photocatalytic semiconductor materials.[40] Figure 5a shows the PL spectra of materials U-LFCN0.66, g-$LaFeO_3$, and s-$LaFeO_3$. According to the analysis of the working principle of the fluorescence luminescence spectrometer, if the PL peak decreases, it means that the energy band structure of the material has changed and the energy difference between electrons and holes has decreased. A smaller energy difference reduces the possibility of spontaneous complexation between electrons and holes.[41] It can be clearly seen that the three catalysts exhibit different degrees of PL emission wave intensities at the wavelengths of 500−700 nm.[42] Among them, the composite catalyst U-LFCN0.66 has a significantly lower photogenerated electron hole complexation rate compared to g-$LaFeO_3$ and s-$LaFeO_3$. This is attributed to the fact that C and N doping altered the charge transport rate of the catalyst $LaFeO_3$ and reduced the photogenerated electron−hole pair complexation, which in turn improved the activity of the catalyst. Figure 5a shows the EIS Nyquist plots of U-LFCN0.66, g-$LaFeO_3$, and s-$LaFeO_3$. The high-frequency part of the Nyquist plots can provide important information about the charge transfer resistance. The charge transfer resistance (R_{ct}) is usually attributed to the semicircle curve in the high-frequency domain. The smaller the semicircle diameter, the higher the conductivity of the semiconductor material, the more efficiently the charge carriers move, the lower the resistance, and the lower the recombination rate of the electron pairs. As shown in Figure 5b, the semicircular diameters of the three materials are, in order, U-LFCN0.66 < g-$LaFeO_3$ < s-$LaFeO_3$. U-LFCN0.66 has the smallest semicircular diameter, and thus, U-LFCN0.66 has a smaller electron transfer resistance. The results of the PL and EIS tests are in accordance with those of the photocatalytic

https://doi.org/10.1021/acsomega.3c06161
ACS Omega 2023, 8, 41744−41754

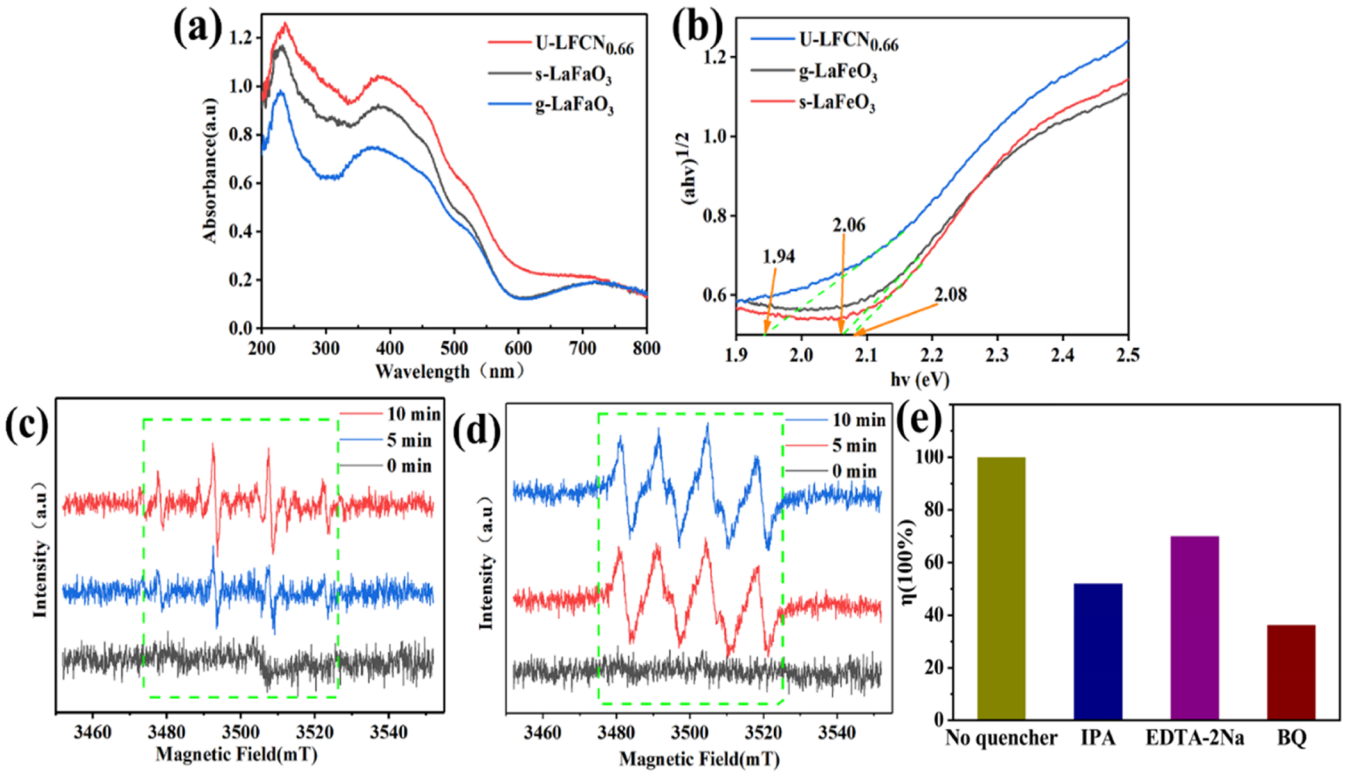

Figure 6. (a, b) UV−Vis absorption spectra of different samples. (c) EPR curves of $^{\bullet}OH$. (d) EPR curves of $^{\bullet}O_2^-$. (e) Degradation of contaminants with the addition of different radical scavengers.

degradation experiments. All of them show that the C- and N-doped $LaFeO_3$ samples can effectively reduce the recombination of photogenerated carriers.

3.6. Active Sites and Catalytic Mechanisms of Catalysts. The UV−visible optical absorption spectra of the samples are shown in Figure 6. The visible absorption fringes of $LaFeO_3$ and its elementally doped materials start at ∼400 nm and end at ∼800 nm, indicating that the $LaFeO_3$-based material significantly displays spectral photoabsorption from UV to visible due to its narrow band gap. Comparison of the UV−visible diffuse reflectance spectra of U-LFCN0.66 and $LaFeO_3$ shows that although pure $LaFeO_3$ shows strong absorption at about 250 and 400 nm, it is significantly weaker than that of the elementally doped material, and the elementally doped material also has a better photoabsorption performance in the visible region at about 600 nm. These are attributed first to the electronic leaps from the O 2p orbitals forming the valence band to the Fe 3d orbitals in the conduction band,[40] and second to the electronic structure changes caused by the distortion of the material's crystal structure and the exposure of more oxygen vacancy sites, as described earlier.[42] The optical band gap of $LaFeO_3$ is calculated using the Tauc relation $(\alpha h\upsilon)^{1/2} = \beta(h\upsilon - E_g)$ (where α is the absorption coefficient, β is a constant dependent on the constant on the hopping probability, and E_g is the optical energy gap). Extrapolation of the linear region shows an optical band gap E_g of about 2.0 eV for $LaFeO_3$ and 1.94 eV for U-LFCN0.66, with a reduced modulation of the band gap, strongly leading to an increase in the spectral response throughout the visible region. In conclusion, the elementally doped sample absorbs significantly more light energy than the other samples, indicating that the reduction in size of the material's specific particle morphology (nano-cylindrical homojunctions of ∼200 nm) and the reduction in the modulation of the band gap lead to a significant redshift of the optical absorption. Therefore, the U-LFCN0.66 photocatalyst prepared by the solid-phase milling method can be used as a potential visible light-driven photocatalyst.

The active species in the photocatalytic degradation of sodium humate were investigated by radical trapping experiments and electron paramagnetic resonance (EPR) studies. In Figure 6c,d, no signal peaks were observed for DMPO−OH and DMPO−O_2^- under dark conditions. In contrast, DMPO−OH and DMPO−O_2^- showed strong signal peaks at 5 min of natural light irradiation, and the signals were even stronger when the irradiation time was extended to 10 min, indicating that $^{\bullet}OH$ and $^{\bullet}O_2^-$ produced during the degradation process were the active species in the photocatalytic degradation of sodium humate and that the $^{\bullet}OH$ and $^{\bullet}O_2^-$ produced were continuous. In addition, by adding isopropanol (IPA), disodium ethylenediaminetetraacetic acid (EDTA-2Na) and p-benzoquinone BQ were used as trappers of hydroxyl radicals ($^{\bullet}OH$), holes (h^+) and superoxide radicals (O_2^-), respectively.[42] The results are shown in Figure 6e, where the degradation rate without any scavenger was 98%. However, the concentration of sodium humate decreased with the addition of EDTA-2Na, indicating that h+ also played a role in the degradation process. In addition, the degradation effect of the catalyst on sodium humate was significantly inhibited by the addition of IPA and BQ, indicating that $^{\bullet}OH$ and O_2^- were the main active species in the degradation process. Therefore, by combining the results of electron spin resonance (EPR) and radical trapping experimental tests, it can be concluded that O_2^- and $^{\bullet}OH$ are the main active species involved in the photocatalytic degradation process.

https://doi.org/10.1021/acsomega.3c06161
ACS Omega 2023, 8, 41744−41754

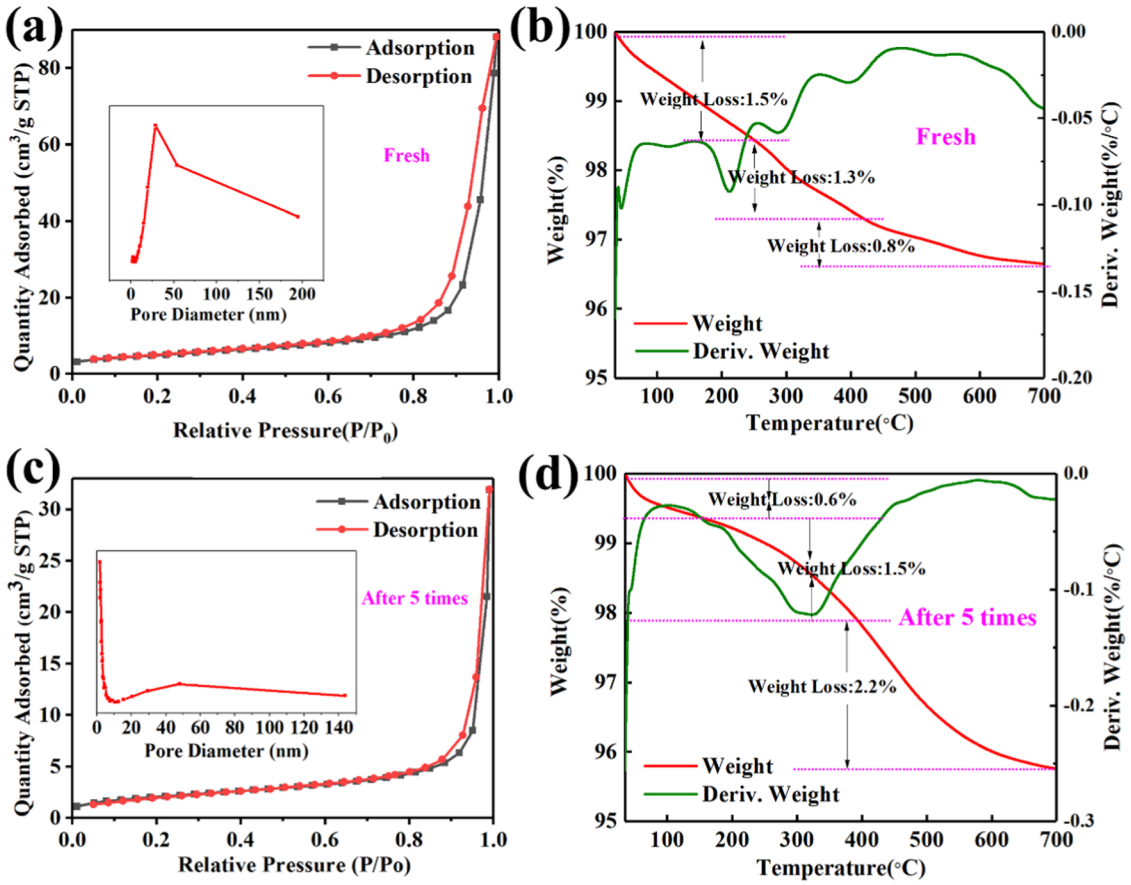

Figure 7. BET and TG-DSC analysis of U-LFCN0.66 catalysts: (a, b) before reaction; (c, d) after reaction.

The changes of the catalyst before and after use were compared by BET and TG-DSC to analyze the catalytic degradation mechanism of the U-LFCN0.66 catalyst more accurately. Figure 7a,b shows the test results of the fresh U-LFCN0.66 catalyst, from which it can be seen that the specific surface area of the U-LFCN0.66 material before use is 17.59 m^2/g, and its average pore size is 25.6 nm. However, the specific surface area of pure phase $LaFeO_3$ prepared by solid-phase milling is 11.09 m^2/g, and its average pore size is 39.2 nm, which indicates that the doping of organic elements increases the catalytic degradation mechanism. This indicates that the doping of organic elements increases the specific surface area of the material, which will be more favorable for the attachment of humic acid molecules during the reaction process. Since the overall material still maintains the rigid structure of ABO_3-type chalcogenide material, its pore size mainly comes from the formation of particle stacking, and the doping of organic elements formed a link between the particles, which resulted in the disappearance of some of the stacking holes, so the pore size of the doped material became smaller. In view of the large size of humic acid molecules, the surface contains numerous polar groups such as carboxyl, amino, and hydroxyl, as well as its colloidal properties; the adsorption of the rest of the material is mainly through the mechanism of hydrogen bonding and electrostatic forces, and in general, the voids of the material and its pore size have little effect on its adsorption. In addition, the pyrolysis process of the fresh U-LFCN0.66 material was smooth, with a total reduction of 3.6% of the total mass from 25 to 700 °C. This may be indicative of the loss of adsorbed water, and the overall thermal stability of the material is strong, representing its structural stability.[43]

In the recycling experiments, we found that the catalytic performance of the material would be greatly reduced; therefore, it was hypothesized that some of the degraded small molecules adhered to the surface of the material, masking some of the catalytic active sites. Based on the above speculation, the specific surface area and pore size distribution of the material after 4 cycles of untreated reaction were tested, and the results are shown in Figure 7c. It is obvious that the specific surface area of the material decreased (7.517 m^2/g) and the pore size distribution broadened; in other words, the mesopores of the material were partially blocked after use. The same result is also confirmed in the TG-DSC results because the thermal decomposition tendency is changed because of the partially degraded organic matter adhered to the surface of the material, and the inflection point occurs at 300 °C. The thermal decomposition tendency of the material is also changed because of the partially degraded organic matter adhering to the surface of the material.[44] Its mass loss within 25−700 °C is 4.3%, which is 0.7% more than the material before use, and this part of the difference may be caused by the pyrolysis of the organic matter attached to the surface.

In the cycling experiments and test analysis before and after material use, we found that some of the large sodium humate molecules would be attached to the surface of the U-LFCN0.66 catalyst as small molecules during the degradation process. This provides the possibility to further investigate the degradation process of sodium humate pollutants. Usually, the degradation process of organic pollutants is difficult to examine

https://doi.org/10.1021/acsomega.3c06161
ACS Omega 2023, 8, 41744−41754

due to low concentrations, insufficient purity of solvents, and other problems. When it was found that some of the postdegradation products might be attached to the catalyst, we sonicated the used catalyst with chromatographically pure methanol, separated and collected the solution, and examined the compounds in it using GC-MS (Table S1). In order to deduct the effect of the catalyst itself and the solvent used in the treatment process, we used the same reagents and methods to treat the fresh U-LFCN0.66 catalyst that had not been in contact with sodium humate as the blank control. After deducting the influence of external environmental factors, although many low molecular weight alcohols and alkanes were found, the total amount of them was very limited, so we believe that only a small portion of the products of the U-LFCN0.66 catalyst, such as low molecular weight alcohols and alkanes, were not completely degraded during the degradation process of sodium humate, while most of the structural groups were completely degraded to inorganic substances such as CO_2 and H_2O.

In summary, we can reasonably speculate on the possible pathways for the degradation of sodium humate by the photocatalyst U-LFCN0.66 (Figure 8). When the catalyst U-LFCN0.66 is irradiated by natural light, electron−hole pairs are generated. The generated electrons are easily captured by water to produce ·OH, while O_2 adsorbed on the surface of U-LFCN0.66 combines with the electrons to form $^{\bullet}O_2^-$. Meanwhile, h^+ itself is an active species that can directly react with the small molecules produced by sodium humate. Finally, all of these active species participate in the degradation process of sodium humate, degrading the large molecules of sodium humate substances adsorbed on the surface of the catalyst to low molecular weight alcohols and alkanes as well as nontoxic small molecules such as CO_2 and H_2O.

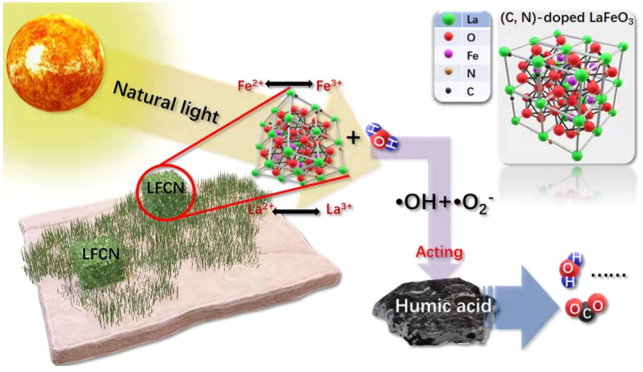

Figure 8. Schematic diagram of the U-LFCN0.66 catalyst for the degradation of sodium humate.

4. CONCLUSIONS

In this article, the preparation process of novel LFCN composites was synthesized using a one-pot method combining solid-phase milling and in situ doping with organic C and N elements, and their removal of sodium humate, a macromolecular organic pollutant in aqueous solution, was investigated. The effects of different doping amounts and different organic dopants on the structure and catalytic performance of the composites were investigated separately, and the results showed that the U-LFCN0.66 catalyst prepared by using urea and chalcocite precursor with a mass ratio of 2:1 had the strongest catalytic performance and the degradation rate of sodium humate could reach 98% of 30 mg/L in 80 mL of sodium humate within 50 min under natural light. Meanwhile, the catalyst was stable enough to be reused more than 4 times and still showed high catalytic activity after 12.5-fold magnification. The XRD and infrared characterization of the materials revealed that different doping amounts and different organics mainly modulated the electronic structure of the composites, thus enhancing their catalytic activities. The catalytic activity of U-LFCN0.66 was enhanced by a factor of 2.88 compared to the pure phase $LaFeO_3$ prepared by conventional sol−gel and solid-phase milling methods, PL suggests that the doping of organic C and N elements adjusted the electronic structure of the ABO_3-type chalcogenide material, thus changing its forbidden bandwidth and enhancing the electron transport. Finally, the catalytic mechanism of the U-LFCN0.66 catalyst in the oxidative degradation of sodium humate was investigated by using EPR, BET, TG-DSC, and GC-MS characterization. The results showed that the U-LFCN0.66 catalyst mainly activated the oxygen in water to generate hydroxyl radicals and superoxide radicals, which degraded the large molecules of sodium humate adsorbed on the surface of the catalyst to low molecular weight alcohols, alkanes, as well as nontoxic small molecules such as CO_2 and H_2O.

■ ASSOCIATED CONTENT

Supporting Information

The Supporting Information is available free of charge at https://pubs.acs.org/doi/10.1021/acsomega.3c06161.

Characterization of photocatalysts and analysis of possible products of oxidative degradation of sodium humate by GC-MS detection of catalysts (PDF)

■ AUTHOR INFORMATION

Corresponding Authors

Zhongzhi Wang − *Baotou Research Institute of Rare Earths, Baotou 014030, China*; Email: 198322wzz@163.com

Xin Qiao − *Baotou Research Institute of Rare Earths, Baotou 014030, China*; Email: qx2113459@qq.com

Authors

Pengcheng Hao − *Baotou Research Institute of Rare Earths, Baotou 014030, China*; orcid.org/0009-0007-5952-1993

Yanli Suo − *Baotou Research Institute of Rare Earths, Baotou 014030, China*

Rui Shi − *Baotou Research Institute of Rare Earths, Baotou 014030, China*

Juan Zhang − *Baotou Research Institute of Rare Earths, Baotou 014030, China*

Bo Li − *Baotou Research Institute of Rare Earths, Baotou 014030, China*

Zhen Yan − *Baotou Research Institute of Rare Earths, Baotou 014030, China*

Jing Wang − *Baotou Research Institute of Rare Earths, Baotou 014030, China*

Bo Liu − *Baotou Research Institute of Rare Earths, Baotou 014030, China*

Complete contact information is available at: https://pubs.acs.org/10.1021/acsomega.3c06161

https://doi.org/10.1021/acsomega.3c06161
ACS Omega 2023, 8, 41744−41754

Author Contributions

P.H.: Conceptualization, Supervision, Editing, Analysis, Validation, Writing, Reviewing. Z.W. and X.Q.: Conceptualization, Methodology, Software, conducting experimental, Analysis, Editing, Reviewing. R.S. and J.Z.: Analysis, Software, Reviewing, Validation. J.W. and B. Liu: Supervision, Reviewing, Validation. Y.S.: Conceptualization, Conducting experimental, Validation. Z.Y.: Software, Reviewing, Validation.

Notes

The authors declare no competing financial interest.

■ ACKNOWLEDGMENTS

This work was financially supported by the Northern Rare Earth Project (No. 2022Z2452).

■ REFERENCES

(1) Turkten, N.; Natali Sora, I.; Tomruk, A.; Bekbolet, M. Photocatalytic Degradation of Humic Acids Using $LaFeO_3$. *Catalysts* **2018**, *8*, 630.

(2) Marwat, M. A.; Humayun, M.; Afridi, M. W.; Zhang, H.; Abdul Karim, M. R.; Ashtar, M.; Usman, M.; Waqar, S.; Ullah, H.; Wang, C.; Luo, W. Advanced Catalysts for Photoelectrochemical Water Splitting. *ACS Appl. Energy Mater.* **2021**, *4*, 12007−12031.

(3) Birben, N. C.; Paganini, M. C.; Calza, P.; Bekbolet, M. Photocatalytic degradation of humic acid using a novel photocatalyst: Ce-doped ZnO. *Photochem. Photobiol. Sci.* **2017**, *16*, 24−30.

(4) Birben, N. C.; Uyguner-Demirel, C. S.; Kavurmaci, S. S.; Gürkan, Y. Y.; Turkten, N.; Cinar, Z.; Bekbolet, M. Application of Fe-doped TiO_2 specimens for the solar photocatalytic degradation of humic acid. *Catal. Today* **2017**, *281*, 78−84.

(5) Zhiyong, Y.; Ruiying, Q.; Runbo, Y.; Zhiyin, W.; Huanrong, L. Photodegradation comparison for methyl orange by TiO_2, H_2O_2 and KIO_4. *Environ. Technol.* **2020**, *41*, 547−555.

(6) Behnajady, M. A.; Dadkhah, H.; Eskandarloo, H. Horizontally rotating disc recirculated photoreactor with TiO(2)-P25 nanoparticles immobilized onto a HDPE plate for photocatalytic removal of p-nitrophenol. *Environ. Technol.* **2018**, *39*, 1061−1070.

(7) Doná, G.; Dagostin, J.; Takashina, T. A.; de Castilhos, F.; Igarashi-Mafra, L. A comparative approach of methylparaben photocatalytic degradation assisted by UV-C, UV-A and Vis radiations. *Environ. Technol.* **2018**, *39*, 1238−1249.

(8) Wang, F.; Wang, W.; Yuan, S.; Wang, W.; Hu, Z. Comparison of UV/H_2O_2 and UV/PS processes for the degradation of thiamphenicol in aqueous solution. *J. Photochem. Photobiol., A* **2017**, *348*, 79−88.

(9) Ofoedu, C. E.; You, L.; Osuji, C. M.; Iwouno, J. O.; Kabuo, N. O.; Ojukwu, M.; Agunwah, I. M.; Chacha, J. S.; Muobike, O. P.; Agunbiade, A. O.; et al. Hydrogen Peroxide Effects on Natural-Sourced Polysacchrides: Free Radical Formation/Production, Degradation Process, and Reaction Mechanism—A Critical Synopsis. *Foods* **2021**, *10*, 699.

(10) Neyens, E.; Baeyens, J. A review of classic Fenton's peroxidation as an advanced oxidation technique. *J. Hazard. Mater.* **2003**, *98*, 33−50.

(11) Zhang, C.; Jiang, S. Applying fenton process in acrylic fiber wastewater treatment and practice teaching. *IOP Conf. Ser.: Earth Environ. Sci.* **2018**, *121*, 032047.

(12) Mu, J.; Feng, J.; Wang, X.; Liu, B. Oxygen vacancy boosting peroxymonosulfate activation over nanosheets assembled flower-like $CoMoO_4$ for contaminant removal: Performance and activity enhancement mechanisms. *Chem. Eng. J.* **2023**, *459*, No. 141537.

(13) Ma, Z.; Yang, K.; Xiao, C.; Jia, L. C-doped $LaFeO_3$ Porous Nanostructures for Highly Selective Detection of Formaldehyde. *Sens. Actuators, B* **2021**, *347*, No. 130550.

(14) Ji, Y.; Xie, Y.; Zheng, L.; Xu, F. Efficient activation of peroxymonosulfate by porous Co-doped $LaFeO_3$ for organic pollutants degradation in water. *J. Solid State Chem.* **2021**, *297*, No. 122077.

(15) Li, Y.; Fan, J.; Feng, X.; Tao, T. Degradation of organics using $LaFeO_3$ as a persulfate activator under low-intensity ultra-violet-light irradiation: Catalytic performance and mechanism. *J. Rare Earths* **2022**, *40*, 1043−1052.

(16) Wang, X.-T.; Li, Y.; Zhang, X.; Li, J.; Li, X.; Wang, C. Design and fabrication of NiS/$LaFeO_3$ heterostructures for high efficient photodegradation of organic dyes. *Appl. Surf. Sci.* **2020**, *504*, No. 144363.

(17) Garcia-Muñoz, P.; Fresno, F.; Ivanez, J.; Robert, D.; Keller, N. Activity enhancement pathways in $LaFeO_3$@TiO_2 heterojunction photocatalysts for visible and solar light driven degradation of myclobutanil pesticide in water. *J. Hazard. Mater.* **2020**, *400*, No. 123099.

(18) Wiranwetchayan, O.; Promnopas, S.; Phadungdhitidhada, S.; Phuruangrat, A.; Thongtem, T.; Singjai, P.; Thongtem, S. Characterization of perovskite $LaFeO_3$ synthesized by microwave plasma method for photocatalytic applications. *Ceram. Int.* **2019**, *45*, 4802−4809.

(19) Lee, H.; Park, Y.; Kim, S.; Kim, B.; Yoon, H.; Jung, S. Rapid degradation of methyl orange using hybrid advanced oxidation process and its synergistic effect. *J. Ind. Eng. Chem.* **2016**, *35*, 205−210.

(20) Xu, C.; Jin, Z.; Yang, J.; Guo, F.; Wang, P.; Meng, H.; Bao, G.; Li, Z.; Chen, C.; Liu, F.; Hu, R. A direct Z-scheme $LaFeO_3$/WO_3 photocatalyst for enhanced degradation of phenol under visible light irradiation. *J. Environ. Chem. Eng.* **2021**, *9*, No. 106337.

(21) Basavarajappa, P. S.; Patil, S. B.; Ganganagappa, N.; Reddy, K. R.; Raghu, A. V.; Reddy, C. V. Recent progress in metal-doped TiO_2, non-metal doped/codoped TiO_2 and TiO_2 nanostructured hybrids for enhanced photocatalysis. *Int. J. Hydrogen Energy* **2020**, *45*, 7764−7778.

(22) Wang, C.; Kang, J.; Sun, H.; Ang, H. M.; Tadé, M. O.; Wang, S. One-pot synthesis of N-doped graphene for metal-free advanced oxidation processes. *Carbon* **2016**, *102*, 279−287.

(23) Hao, P.; Lin, Z.; Song, P.; Yang, Z.; Wang, Q. rGO-wrapped porous $LaFeO_3$ microspheres for high-performance triethylamine gas sensors. *Ceram. Int.* **2020**, *46*, 9363−9369.

(24) Chen, X.; Zhang, M.; Qin, H.; Zhou, J.; Shen, Q.; Wang, K.; Chen, W.; Liu, M.; Li, N. Synergy effect between adsorption and heterogeneous photo-Fenton-like catalysis on $LaFeO_3$/lignin-biochar composites for high efficiency degradation of ofloxacin under visible light. *Sep. Purif. Technol.* **2022**, *280*, No. 119751.

(25) Pang, X.; Guo, Y.; Zhang, Y.; Xu, B.; Qi, F. $LaCoO_3$ perovskite oxide activation of peroxymonosulfate for aqueous 2-phenyl-5-sulfobenzimidazole degradation: Effect of synthetic method and the reaction mechanism. *Chem. Eng. J.* **2016**, *304*, 897−907.

(26) Humayun, M.; Qu, Y.; Raziq, F.; Yan, R.; Li, Z.; Zhang, X.; Jing, L. Exceptional Visible-Light Activities of TiO_2-Coupled N-Doped Porous Perovskite $LaFeO_3$ for 2,4-Dichlorophenol Decomposition and CO_2 Conversion. *Environ. Sci. Technol.* **2016**, *50*, 13600−13610.

(27) Jones, A.; Islam, M. S. Atomic-Scale Insight into $LaFeO_3$ Perovskite: Defect Nanoclusters and Ion Migration. *J. Phys. Chem. C* **2008**, *112*, 4455−4462.

(28) Phan, T. T. N.; Nikoloski, A. N.; Bahri, P. A.; Li, D. Optimizing photocatalytic performance of hydrothermally synthesized $LaFeO_3$ by tuning material properties and operating conditions. *J. Environ. Chem. Eng.* **2018**, *6*, 1209−1218.

(29) Wu, Y.; Wang, H.; Tu, W.; Liu, Y.; Tan, Y. Z.; Yuan, X.; Chew, J. W. Quasi-polymeric construction of stable perovskite-type $LaFeO_3$/g-C_3N_4 heterostructured photocatalyst for improved Z-scheme photocatalytic activity via solid p-n heterojunction interfacial effect. *J. Hazard. Mater.* **2018**, *347*, 412−422.

(30) Li, Y.; Tang, S.; Sheng, H.; Li, C.; Li, H.; Dong, B.; Cao, L. Multiple roles for LaFeO3 in enhancing the Photoelectrochemical performance of WO_3. *J. Colloid Interface Sci.* **2023**, *629*, 598−609.

(31) Yao, Q.; Tian, C.; Lu, Z.; Wang, J.; Zhou, H.; Rao, G. Antiferromagnetic-ferromagnetic transition in Bi-doped $LaFeO_3$ nanocrystalline ceramics. *Ceram. Int.* **2020**, *46*, 20472−20476.

https://doi.org/10.1021/acsomega.3c06161
ACS Omega 2023, 8, 41744−41754

(32) Jing, J.; Cao, C.; Ma, S.; Li, Z.; Qu, G.; Xie, B.; Jin, W.; Zhao, Y. Enhanced defect oxygen of $LaFeO_3$/GO hybrids in promoting persulfate activation for selective and efficient elimination of bisphenol A in food wastewater. *Chem. Eng. J.* **2021**, *407*, No. 126890.
(33) Frankowski, R.; Płatkiewicz, J.; Stanisz, E.; Grześkowiak, T.; Zgoła-Grześkowiak, A. Biodegradation and photo-Fenton degradation of bisphenol A, bisphenol S and fluconazole in water. *Environ. Pollut.* **2021**, *289*, No. 117947.
(34) Das, K. C.; Dhar, S. S. Rapid catalytic degradation of malachite green by $MgFe_2O_4$ nanoparticles in presence of H_2O_2. *J. Alloys Compd.* **2020**, *828*, No. 154462.
(35) Marwat, M. A.; Ullah, H.; Usman, M.; Ehsan, M. A.; Zhang, H.; Khan, M. F.; Ali, S.; Yousaf, M. Significantly improved photocatalytic activity of the SnO_2/$BiFeO_3$ heterojunction for pollutant degradation and mechanism. *Ceram. Int.* **2022**, *48*, 14789−14798.
(36) Kwan, P. P.; Banerjee, S.; Shariff, M.; Yusoff, F. M. Persistence of malachite green and leucomalachite green in red tilapia (Oreochromis hybrid) exposed to different treatment regimens. *Food Control* **2020**, *108*, No. 106866.
(37) Pan, K.; Yang, C.; Hu, J.; Yang, W.; Liu, B.; Yang, J.; Liang, S.; Xiao, K.; Hou, H. Oxygen vacancy mediated surface charge redistribution of Cu-substituted $LaFeO_3$ for degradation of bisphenol A by efficient decomposition of H_2O_2. *J. Hazard. Mater.* **2020**, *389*, No. 122072.
(38) Yuan, H.; He, Z. Integrating membrane filtration into bioelectrochemical systems as next generation energy-efficient wastewater treatment technologies for water reclamation: A review. *Bioresour. Technol.* **2015**, *195*, 202−209.
(39) Coccia, F.; Tonucci, L.; Bosco, D.; Bressan, M.; D'Alessandro, N. One-pot synthesis of lignin-stabilised platinum and palladium nanoparticles and their catalytic behaviour in oxidation and reduction reactions. *Green Chem.* **2012**, *14*, 1073.
(40) Adeel, M.; Saeed, M.; Khan, I.; Muneer, M.; Akram, N. Synthesis and Characterization of Co−ZnO and Evaluation of Its Photocatalytic Activity for Photodegradation of Methyl Orange. *ACS Omega* **2021**, *6*, 1426−1435.
(41) Kong, L.; Mu, X.; Fan, X.; Li, R.; Zhang, Y.; Song, P.; Ma, F.; Sun, M. Site-selected N vacancy of g-C3N4 for photocatalysis and physical mechanism. *Appl. Mater. Today* **2018**, *13*, 329−338.
(42) Wang, Y.; Wang, Q.; Zhang, H.; Wu, Y.; Jia, Y.; Jin, R.; Gao, S. CTAB-assisted solvothermal construction of hierarchical Bi_2MoO_6/Bi_5O_7Br with improved photocatalytic performances. *Sep. Purif. Technol.* **2020**, *242*, No. 116775.
(43) Hema, E.; Manikandan, A.; Karthika, P.; Antony, S. A.; Venkatraman, B. R. A Novel Synthesis of Zn^{2+}-Doped $CoFe_2O_4$ Spinel Nanoparticles: Structural, Morphological, Opto-magnetic and Catalytic Properties. *J. Supercond. Novel Magn.* **2015**, *28*, 2539−2552.
(44) He, J.; Yang, X.; Men, B.; Bi, Z.; Pu, Y.; Wang, D. Heterogeneous Fenton oxidation of catechol and 4-chlorocatechol catalyzed by nano-Fe_3O_4: Role of the interface. *Chem. Eng. J.* **2014**, *258*, 433−441.

https://doi.org/10.1021/acsomega.3c06161
ACS Omega 2023, 8, 41744−41754